Atomic layer deposition of h-BN(0001) multilayers on Ni(111) and chemical vapor deposition of graphene on h-BN(0001)/Ni(111)

Jessica Jones, Aparna Pilli, Veronica Lee, John Beatty,[a] Brock Beauclair,[b] Natasha Chugh,[c] and Jeffry Kelber[d]
Department of Chemistry, University of North Texas, Denton, Texas 76203

In situ direct, epitaxial growth of multilayers of hexagonal boron nitride (h-BN) and graphene without physical transfer is of significant interest for the scalable production of graphene/h-BN heterostructures for device applications. Deposition on magnetic substrates is of particular interest for spin tunneling applications. X-ray photoelectron spectroscopy and low energy electron diffraction demonstrate epitaxial atomic-layer deposition (ALD) of multilayer h-BN(0001) on Ni(111) and subsequent deposition of azimuthally-aligned multilayer graphene on h-BN(0001)/Ni(111) by chemical vapor deposition. Boron nitride ALD was accomplished with alternating cycles of BCl_3/NH_3 at a 600 K substrate temperature, and subsequent annealing in ultrahigh vacuum. Subsequent deposition of graphene was achieved by chemical vapor deposition using ethylene (CH_2CH_2) at 1000 K. *Published by the AVS.* https://doi.org/10.1116/1.5120628

I. INTRODUCTION

Direct, epitaxial growth of hexagonal boron nitride [h-BN(0001)] and graphene by industrially scalable methods is of critical interest for a variety of device applications.[1–4] This includes tunneling spin filters, in which the predicted tunneling magnetoresistance depends directly on rigorous azimuthal alignment between Ni or Co electrodes and BN and/or graphene layers, as well as the number of aligned BN and graphene monolayers (MLs).[3–5] h-BN and Ni (111) have a close in-plane lattice match (2.50 and 2.49 Å, respectively)[6,7] making Ni(111) a good magnetic substrate for direct growth of h-BN. h-BN and graphene also have a very close lattice match (∼1.7% mismatch),[8,9] which allows for a theoretically flat surface and low lattice strain for graphene. Atomic-layer deposition (ALD) of h-BN allows for ML control over the thickness of the epitaxial layers, which offers clear advantages for some applications.[3,10] ALD is a very specific type of chemical vapor deposition (CVD) where ALD is defined as sequential self-limiting, solid-gas reactions used to accomplish conformal atomic-layer thickness control.[11] This is in contrast to CVD, where the thickness is not inherently self-limiting but dependent on the time and pressure of the precursor(s) exposure and the temperature of the substrate, among other factors such as chemical interactions.[12–15] For example, CVD of graphene is normally accomplished by exposing a substrate to a hydrocarbon such as methane or ethylene at high temperatures (∼1000 K) where the precursor decomposes on the surface to provide a source of C where the thickness is dependent on the time and pressure of hydrocarbon used.[12,13]

Applications for ALD in the literature include membranes,[16] photovoltaics,[17] water purification,[18] biosensors,[19] microelectronics,[20] and spintronics.[2,5] ALD applications for BN have been widely reported in the literature; B_2O_3 capped with BN for Si doping,[21,22] BN grown using PEALD for capacitors,[20] BN nanotubes for water purification,[18] and possible spintronic devices.[2,5,23,24] BN has been proposed for a variety of applications within spintronics, including minority spin filtering for spin injection for magnetic tunnel junctions,[2,5,23,24] and as the dielectric for a nonlocal spin valve.[23] ALD gives the atomic-layer control needed for fabrication of spintronic devices such as magnetic tunnel junctions using Al_2O_3 (Ref. 25) or h-BN (Refs. 2 and 5) because spin devices rely heavily on atomically thin films.[25] The precise control over film thickness inherent to ALD, as well as the resulting azimuthal alignment between layers, make this method attractive for device fabrication, especially since multilayers of h-BN are superior to monolayers for certain spin injection applications.[24,25]

Previously, several attempts were made to deposit multilayer, epitaxial h-BN on Ni(111) (in addition to exfoliation methods). h-BN deposition has been achieved by borazine pyrolysis at substrate temperatures ranging from 973 to 1073 K.[26,27] Growth by this method was found to be polycrystalline after the first ML as indicated by the absence of low energy electron diffraction (LEED) spots.[27] Significant orbital hybridization between the Ni and h-BN π bands on monolayer h-BN grown by CVD of borazine has previously been demonstrated.[27,28] Multilayer growth of h-BN was achieved using molecular beam epitaxy (MBE), but precise control over the thickness using MBE is difficult.[29,30] Other deposition methods like magnetron sputtering[31] and pulsed laser deposition[32] do not provide atomic-layer control of h-BN growth. ALD of h-BN allows for epitaxial, multilayer growth, unlike growth by borazine CVD, which is largely self-limiting to 1 ML, for epitaxial h-BN.[6,26,28,33,34] Here, we report (for the first time) epitaxial, multilayer h-BN deposited on Ni(111) by ALD and the subsequent growth of azimuthally-aligned graphene by CVD.

---

[a]Present address: Department of Chemistry, Texas Womens University, Denton, TX 76203.
[b]Present address: Department of Physics, Purdue University, West Lafayette, IN 47907.
[c]Present address: Department of Biomedical Engineering, Johns Hopkins University, Baltimore, MD 21218.
[d]Author to whom correspondence should be addressed: Kelber@unt.edu

A number of precursors have been used for the ALD of BN on various substrates, such as Al_2O_3, Si, and SiO_2.[20,35–37] The use of BBr_3 and NH_3 as precursors has been reported at substrate temperatures ranging from 673 to 1023 K, which resulted in turbostratic growth.[18,35,38,39] This was followed by other reports using the same precursors for laser-assisted ALD of BN on SiO_2, also resulting in turbostratic growth of BN.[36] Thermal and plasma-assisted ALD of BN using noncorrosive precursors has also been established. Triethylborane and NH_3 (Ref. 37) were used to deposit BN on Si and Al_2O_3 between 770 and 1170 K, which at lower temperatures resulted in amorphous BN, but at higher temperatures resulted in sp^2 BN, but the process was no longer self-limiting above 873 K. Triethylborate and N_2/H_2 plasma[20] were used in plasma-assisted ALD to grow h-BN between 470 and 620 K.

The ALD process reported here uses alternating exposures of BCl_3 and NH_3 at 600 K, similar to that employed for multilayer h-BN(0001) growth on Co(0001),[10,40] RuO_2(110)/Ru(0001),[41] ZrO_2,[42] and on B_2O_3/Si(100).[22] A schematic of this reaction is presented in Fig. S1 in the supplementary material.[55] This chemistry is robust for h-BN deposition on transition metals, oxides of main group elements, and transition metal oxides. Here, x-ray photoelectron spectroscopy (XPS) and LEED data are presented, demonstrating layer-by-layer, epitaxy of h-BN(0001) on a Ni(111) single crystal. The data indicate that the BN lattice is aligned with the Ni substrate and that graphene subsequently deposited by CVD is epitaxially deposited on and azimuthally aligned with the h-BN.

II. EXPERIMENT

A $5 \times 5 \times 0.5$ mm^3 Ni(111) single crystal was obtained from commercial vendors and was introduced into a multichamber vacuum system described elsewhere.[10,21] Briefly, the system included a turbomolecularly pumped chamber for ALD (base pressure 3×10^{-6} Torr), a turbomolecularly pumped chamber for XPS, reverse-view LEED, and Ar^+ ion sputter gun for sample cleaning in UHV (base pressure 1×10^{-10} Torr) separated by manually operated gate valves. The ALD chamber is equipped with a manually operated butterfly valve that allows the chamber to be closed to the turbo pump, and a dedicated rough pump that creates a flow through of the gasses during exposures, allowing pressurization of the chamber to hundreds of millitorr. Pressures in the ALD chamber were recorded by a combination of nude ion gauge to measure pressures in the high vacuum regime and baratron gauge to measure pressures at higher pressures between 1 mTorr and 1 Torr. Pressures in UHV were recorded with a nude ion gauge calibrated for N_2. Sample temperatures in each chamber were varied by resistive heating and measured by a K type thermocouple mounted on the sample stage near the sample. Heating in the ALD chamber occurred with the use of a ceramic-encapsulated heater designed for use in reactive environments. Samples were transported between the chambers without exposure to ambient conditions via of a magnetically coupled feedthrough. A detailed schematic of this multichamber system can be found elsewhere.[21]

XPS data were acquired with a 100 mm mean radius hemispherical analyzer operating at a constant pass energy (50 eV), with nonmonochromatic Al Kα x-ray source operated at 15 keV, 300 W. XPS spectra were analyzed with commercially available software and all spectral binding energies were calibrated to that of metallic Ni $2p_{3/2}$ at 852.7 eV. Relative atomic concentrations and thicknesses were calculated by standard methods[43] using inelastic mean free paths (IMFPs) of Ni through BN, B through BN, and N through BN of 19.98, 29.48, and 30.05 Å, respectively. The thickness of graphene was determined by the IMFP of B, N, and C through graphene 32.63, 28.49, and 30.79 Å, respectively.[44] The XPS-derived thickness of BN and graphene monolayers was taken to be 3.3 and 3.35 Å, respectively, in agreement with previous STM studies of multilayer BN on Ru(0001)[45] and of multilayer graphene.[46] A commercial three grid reverse-view LEED apparatus was used to collect LEED images, which were captured from 300 to 60 eV on all samples.

The $5 \times 5 \times 0.5$ mm^3 Ni(111) single crystal was cleaned *in situ* by annealing in O_2 (10^{-7} Torr, 1000 K; Air Gas, 99.999% purity, CAS No. 7752-44-7) to remove adventitious C. Ni substrates were subsequently exposed to a flux of Ar^+ ions (Scott Specialty Gases, 99.9999% purity, CAS No. 7440-37-1) at a pressure of 5×10^{-5} Torr, a beam energy of 3 keV, and a beam current of 25 mA to remove the surface oxygen. The crystal was then annealed repeatedly to 1000 K in UHV to remove any residual contamination as determined by XPS and to order the surface until a well-defined hexagonal LEED pattern was obtained. The relatively small size of the sample, combined with an analyzer source area of $\sim 1 \times 5$ mm^2, resulted in some Ta 4p intensity present in N 1s spectra. This did not, however, impact any of the conclusions presented here.

Electronic grade BCl_3 (IGX Group, CAS No. 10294-34-5, 99.999% purity) and NH_3 (Praxair, CAS No. 7664-41-7, >99.999% purity) gases were used as precursors without further purification. The turbo pump to the deposition chamber was closed off during each exposure, and a dedicated roughing pump was used to create a flow-through system during exposures. BCl_3 exposures were at 250 mTorr for 5 min, and NH_3 exposures were at 350 mTorr for 2 min, all at 600 K. Between BCl_3 and NH_3 exposures, the rough pump was closed off and the turbo pump was reopened for 2 min to the system to allow any excess gas to be pumped away.

Graphene growth was accomplished by heating the substrate to 1000 K and then exposing the sample to 100 mTorr CH_2CH_2 (Matheson, CAS No. 74-85-1, 99.999% purity) for 23 min. In this case, the substrate consisted of Ni(111) with 2 ML of h-BN(0001) deposited by ALD, as this BN thickness has been suggested as optimal for certain spin filter applications.[5]

III. RESULTS AND DISCUSSION

A. ALD of h-BN(0001) on Ni(111)

XPS spectra of B 1s and Cl 2p, N 1s, Ta $4p_{3/2}$, and Ni $2p_{3/2}$ regions are shown in Figs. 1(a)–1(c), respectively, after
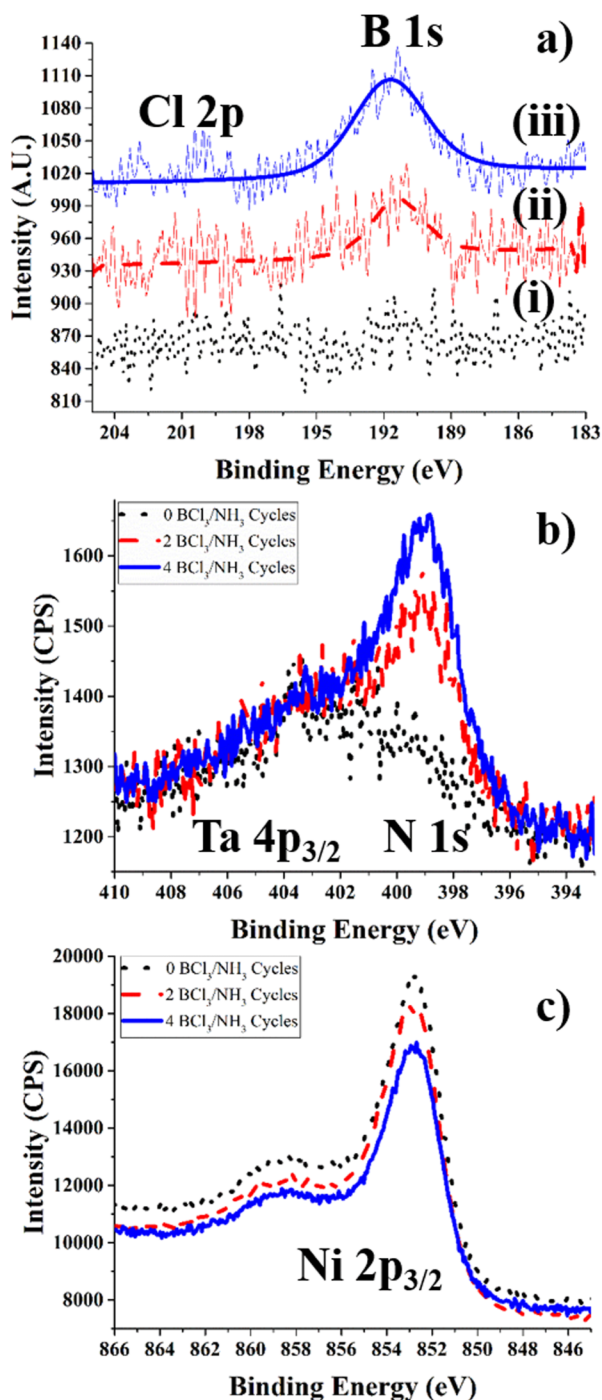
FIG. 1. XPS spectra of (a) B 1s and Cl 2p (i) before BCl_3/NH_3 cycles (black dot trace), (ii) after two BCl_3/NH_3 cycles + 1000 K UHV anneal; fit of B 1s (red dash trace) and corresponding raw data (thin red line), and (iii) after four BCl_3/NH_3 cycles + 1000 K UHV anneal; fit of B 1s (blue solid trace) and corresponding raw data (thin blue line), (b) N 1s and Ta $4p_{3/2}$ before BCl_3/NH_3 cycles (black dot trace), after two BCl_3/NH_3 cycles + 1000 K UHV anneal (red dash trace), and after four BCl_3/NH_3 cycles + 1000 K UHV anneal (blue solid trace), (c) Ni $2p_{3/2}$ before BCl_3/NH_3 cycles (black dot trace), after two BCl_3/NH_3 cycles + 1000 K UHV anneal (red dash trace), and after four BCl_3/NH_3 cycles + 1000 K UHV anneal (blue solid trace).

0, 2, and 4 cycles of BCl_3/NH_3 at 600 K and subsequent UHV anneals to 1000 K to remove chlorine contamination. Figure 1(a) shows an increase in the intensity of B 1s at ~191 eV with increasing number of BCl_3/NH_3 reaction

cycles. This binding energy is consistent with BN formation.[22,41,47,48] UHV anneals to 1000 K reduced Cl impurities to <3 at. %. Figure 1(b) shows N 1s growth at ~398 eV, also consistent with BN formation.[22,41,47,48] Ta is also observed in this sample [near 401 eV, Fig. 1(b)]. The breadth of the Ta $4p_{3/2}$ feature indicates both metallic and oxidized Ta. The attenuation in the Ni $2p_{3/2}$ signal [Fig. 1(c)] was used to calculate the thickness of the h-BN film through both B 1s and N 1s.

Chlorine removal at 1000 K in UHV after two cycles BCl_3/NH_3 at 600 K is shown in Fig. 2(a). The intensity of the B 1s peak slightly decreases and shifts to a lower binding energy after a 3 h 1000 K UHV anneal, indicating some desorption of undissociated or partially dissociated BCl_x from the surface. After this anneal, the N 1s peak [Fig. 2(b)] narrows significantly at ~398 eV, consistent with h-BN formation.[10,40,41] The full width at half maximum (FWHM) of the N 1s component of the region narrows from 4.2 eV after deposition to 3.2 eV after 3 h of 1000 K anneals in UHV. These data indicate a reduction in the number of bonding environments, possibly due to desorption of some partially dissociated NH_y or the conversion of some partially reacted BCl_x and NH_y to h-BN and HCl gas. Annealing in UHV
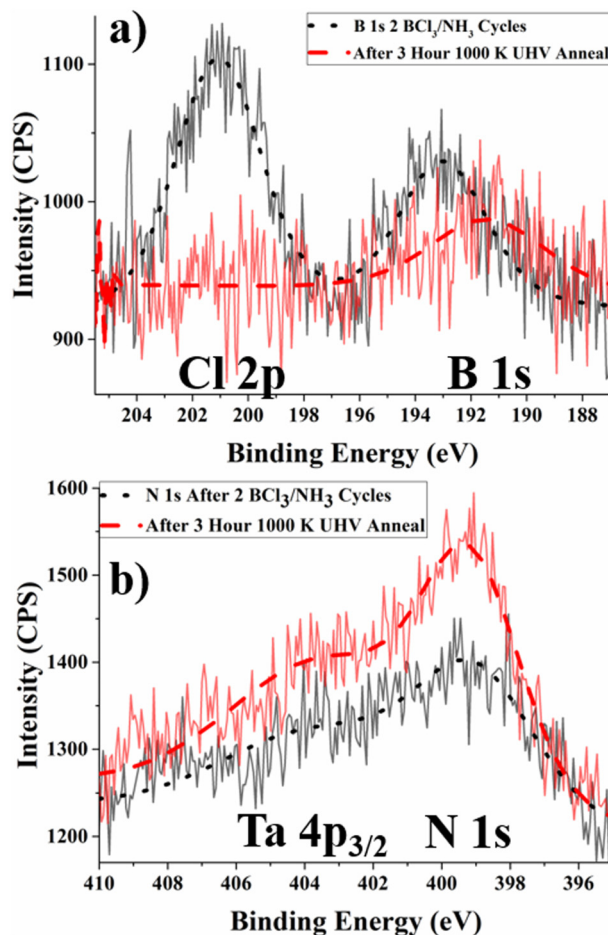

FIG. 2. XPS spectra of (a) B 1s and Cl 2p regions and (b) N 1s and Ta $4p_{3/2}$ regions after 2 cycles BCl_3/NH_3 at 600 K; sum of components (black dot trace), with corresponding raw data (thin black trace), and subsequent UHV 3 h anneal to 1000 K sum of components (red dash trace), with corresponding raw data (thin red trace).

resulting in removal of Cl from the film is necessary to ensure a high quality, pure h-BN film with minimal contamination, in rigorous azimuthal alignment with the substrate, which would be necessary for device applications.[2,5,23,24] Figure 2(b) shows that the intensities of both N 1s and Ta $4p_{3/2}$ features increased upon annealing. This is likely due to Ta metal's relative chemical inertness, indicating that after 1000 K UHV anneal any adsorbed BCl_3 or NH_3 on the Ta desorbed from the Ta straps holding the sample to the holder.

Figure 3(a) shows the average XPS-derived thicknesses of h-BN deposited on Ni(111) by BCl_3/NH_3 at 600 K on three different, identically prepared sample surfaces. In each case, the single crystal was cleaned by Ar^+ ion sputtering and annealing in O_2 and in UHV, before exposures to BCl_3/NH_3 at 600 K. For one sample (designated Sample 1), the single crystal was exposed to two cycles BCl_3/NH_3 at 600 K. For the second ALD process, the clean single crystal was exposed to two, then to an additional two cycles BCl_3/NH_3 at 600 K (designated Sample 2). For the third study, the clean surface was exposed to four, then to an additional four cycles BCl_3/NH_3 at 600 K (designated Sample 3).

The average thickness of h-BN was found by the attenuation of Ni $2p_{3/2}$ through both B 1s and N 1s, and error was
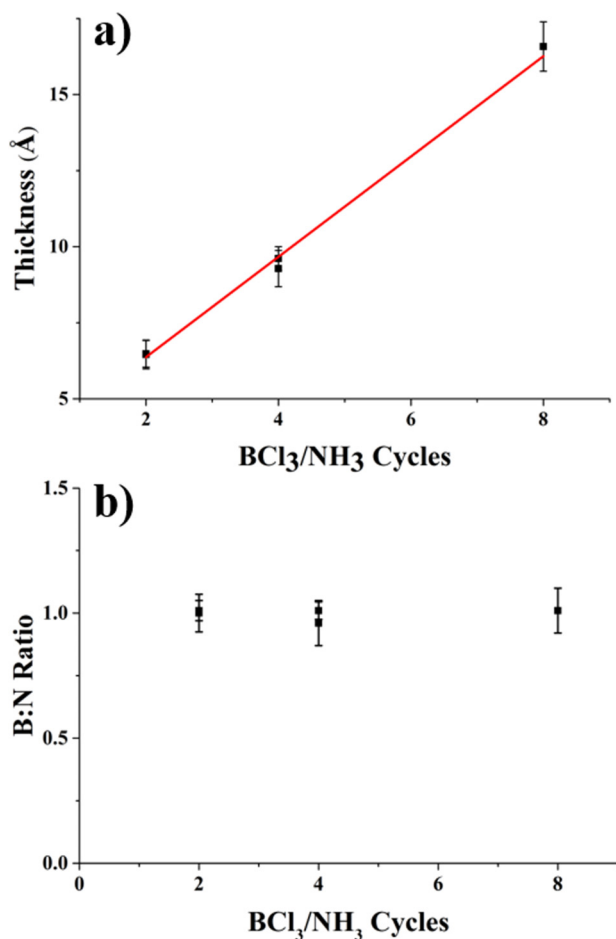

FIG. 3. (a) Plot of XPS-derived average thickness of BN and (b) B:N atomic ratios after 2, 2, 4, 4, and 8 BCl_3/NH_3 exposures at 600 K followed by UHV anneals vs number of BCl_3/NH_3 cycles at 600 K. The solid line in (a) is a least-squares fit to the data.

TABLE I Summary of B 1s and N 1s binding energies during depositions.

Sample	BCl_3/NH_3 cycle	B 1s	N 1s	Δ
Sample 1	2 Cycles	191.4	398.7	207.4
Sample 2	2 Cycles	191.4	399.0	207.6
	4 Cycles	191.8	399.0	207.2
Sample 3	4 Cycles	192.0	399.0	206.9
	8 Cycles	192.0	399.0	206.9

determined from the standard deviation of this average. There is a high level of consistency between samples, reflected by the nearly identical thicknesses determined for identical reaction cycles carried out on different surfaces [Fig. 3(a)]. The linear fit of the data in Fig. 3(a) is consistent with an ALD process, but has a y-intercept of 3.07 ± 0.24 Å with an indicated growth rate of 1.65 ± 0.07 Å/cycle. This growth rate is consistent with other reports of BN deposition on B_2O_3/Si,[22] Co(0001),[40] and ZrO_2.[42] This nonzero y-intercept of the linear regression of thickness versus cycle [Fig. 3(a)] indicates that BCl_3/NH_3 has a higher sticking coefficient on the bare Ni(111) surface than on h-BN, consistent with previous reports of BN growth by ALD of h-BN on RuO_2/Ru,[41] and Co (0001)[40] and by magnetron sputter deposition on Ru.[31] Figure 3(b) shows the B:N atomic ratio corresponding to each of the thickness calculations. The atomic ratio stays very close to 1:1, indicating linear, stoichiometric growth of h-BN.

Table I shows the binding energies of the B 1s and N 1s with an average uncertainty of ±0.3 eV and the difference (Δ) between those binding energies after completion of different numbers of BCl_3/NH_3 cycles. The B 1s binding energy shifts to higher binding energy with increasing numbers of cycles, while the N 1s remains essentially constant. The Δ values between B 1s and N 1s are generally consistent with other reports of h-BN ALD by BCl_3/NH_3,[10,22,40,41] but are somewhat smaller than those reported for BN grown by CVD methods.[49,50] Δ shifts to lower values because the binding energy of B 1s increases from 2 to 4 cycles. The different behaviors of the B 1s and N 1s binding energies with film thickness demonstrate that this is not a result of the p-type band bending theorized for h-BN on Ni.[51] The B 1s shift to higher binding energies with increasing BN thickness is instead consistent with some Ni → B charge transfer at the interface that does not extend to subsequently grown layers.

B. CVD of graphene on h-BN(0001)/Ni(111)

Figure 4 shows XPS spectra of C 1s, B 1s, Cl 2p, and the N 1s/ Ta $4p_{3/2}$ regions before and after graphene CVD with no subsequent UHV anneals, on a 2 ML thick h-BN film on Ni(111) (Sample 1). Figure 4(a,ii) shows the increase in carbon at a peak binding energy of ~284.5 eV corresponding to sp^2 carbon.[52] The FWHM of the C 1s region after CVD (~3.5 eV) is somewhat broad, consistent with the persistence of adventitious C (~285.6 eV) present before CVD as shown in Fig. 4(a,i).[52] Using this deconvolution, the average thickness of the graphene layer calculated using the ratio of the
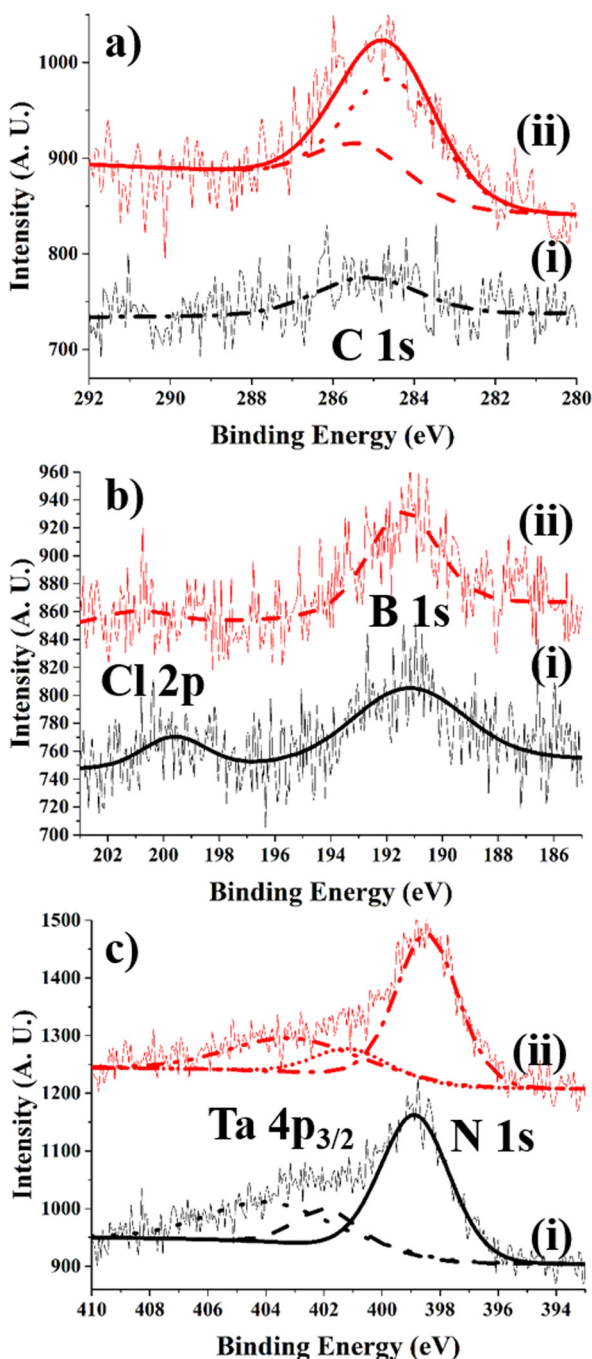
FIG. 4. XPS spectra of (a) C 1s after (i) ALD of h-BN showing adventitious carbon (black dot-dashed trace) with corresponding raw data (thin black trace), (ii) C 1s after CVD showing sp^2 C 1s (red dot trace), adventitious carbon (red dashed trace), and sum of components (solid red trace) with corresponding raw data (thin red trace); (b) B 1s and Cl 2p, (i) sum of components after ALD (black solid trace), with corresponding raw data (thin black trace) and (ii) sum of components after CVD (red dash trace), with corresponding raw data (thin red trace); (c) N 1s and Ta 4p$_{3/2}$ (i) after ALD showing N 1s (solid black trace), Ta 4p$_{3/2}$ metallic (black dash trace), Ta 4p$_{3/2}$ oxidized (black dot trace), with corresponding raw data (thin black trace) and (ii) after CVD showing N 1s (red dot-dashed trace), Ta 4p$_{3/2}$ metallic (red small-dot trace), Ta 4p$_{3/2}$ oxidized (red dash-dot-dot trace), with corresponding raw data (thin red trace).

intensities of B 1s and N 1s through the C 1s was 10.9 ± 0.7 Å (~3 ML).

Figure 4(b) shows a narrowing of B 1s region and a further reduction in the area of the Cl 2p region after CVD.
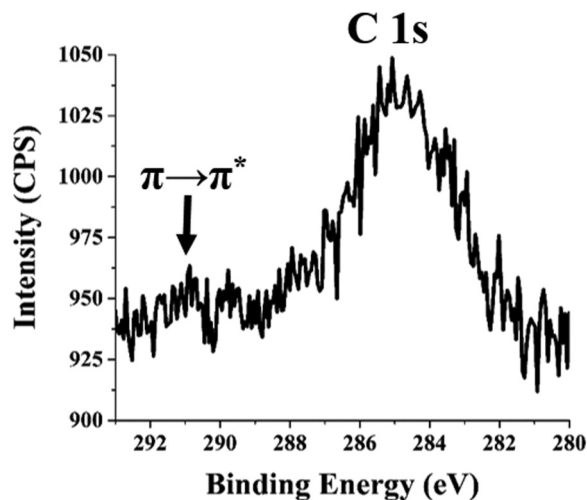

FIG. 5. XPS of C 1s after CVD (100 mTorr, 23 min CH$_2$CH$_2$ exposure at 1000 K) and subsequent UHV anneals to 1000 K.

This could be from a reaction of H from the ethylene with any remaining Cl when the graphene was deposited on the surface, or simply Cl removal by heating to 1000 K during the CVD process, similar to the effect demonstrated in Fig. 2(a). Figure 4(c) shows the N 1s and Ta 4p$_{3/2}$ region before and after CVD. The N 1s region also narrowed and shifted downward in binding energy upon CVD, which could be due to the removal of H incorporated in the film (BNH$_2$ or B$_2$NH)[42] from the high temperature used for CVD or a reaction with desorbed Cl species to produce HCl. The Ta 4p$_{3/2}$ regions also shifted lower in binding energy, possibly as a result of H from ethylene reducing the oxidation of the Ta straps used in mounting the sample. Overall, the data in Fig. 4 demonstrate that the 2 ML thick h-BN was intact after graphene CVD. Figure 5 displays in detail the C 1s spectrum after ethylene CVD and UHV anneals to order the surface. These data are shown to highlight the $\pi \rightarrow \pi^*$ shake up at 291 eV, corroborating the sp^2 nature of the deposited C layer.

LEED data of the Ni(111) surface before and after h-BN deposition, and after graphene CVD, are displayed in Figs. 6(a)–6(c), respectively. These data, all acquired at the same beam energy of 80 eV, demonstrate that the surface lattice remains hexagonal with approximately constant lattice spacing, as expected for a graphene/BN/Ni(111) heterostructure. These data, however, also demonstrate that the h-BN
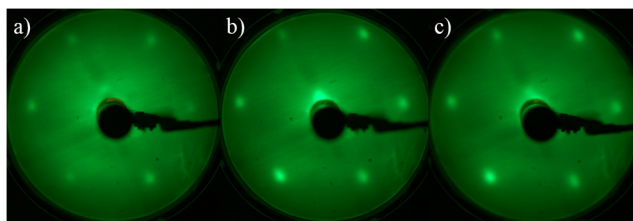

FIG. 6. LEED images at 80 eV of (a) clean Ni(111) single crystal, (b) of h-BN after two cycles BCl$_3$/NH$_3$ cycles at 600 K and UHV anneals, and (c) graphene after CVD and UHV anneals at 1000 K.
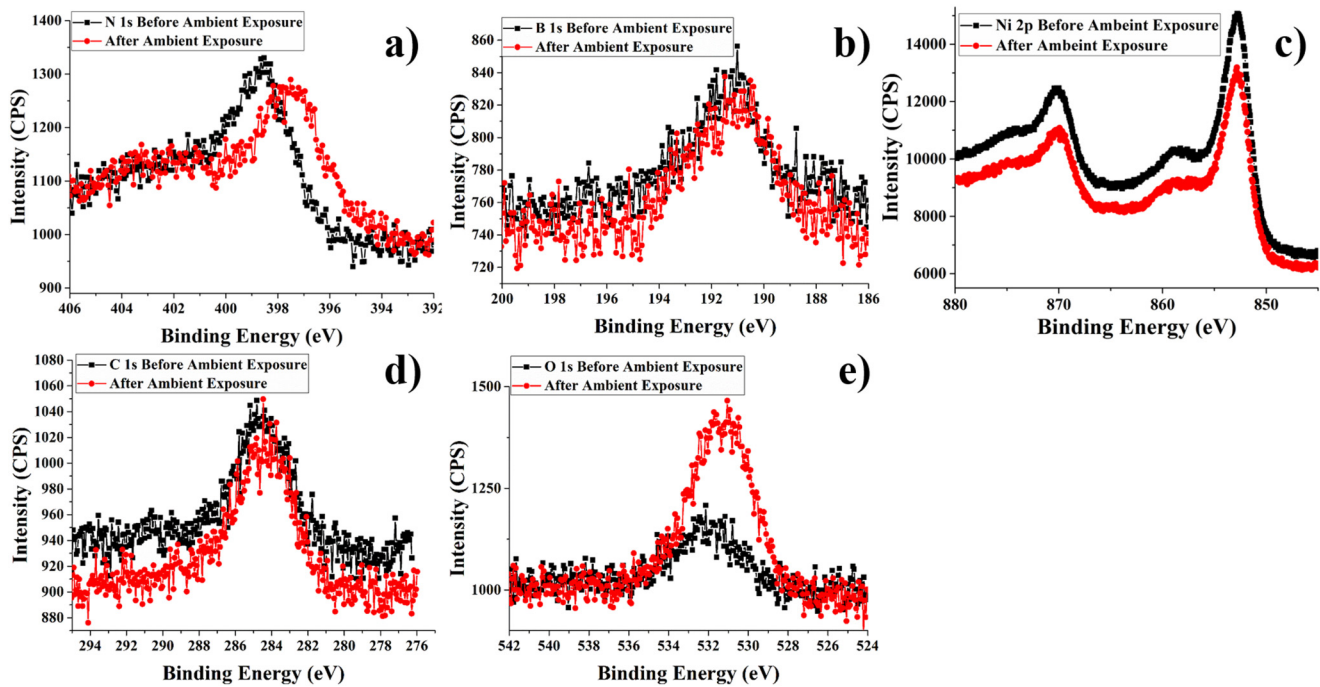
FIG. 7. XPS spectra of (a) N 1s, Ta 4p 3/2, (b) B 1s, Cl 2p, (c) Ni 2p, (d) C 1s, and (e) O 1s before ambient exposure (black square trace) and after ambient exposure (red circle trace).

lattice [Fig. 6(b)] and graphene lattice [Fig. 6(c)] remain in close azimuthal alignment with the lattice of the Ni(111) surface. Such an azimuthal alignment is critical for the "Brillouin zone spin-filtering mechanism" proposed for Ni(111) [or Co(0001)]/BN/graphene spin filters.[4]

C. Ambient exposure of graphene/BN/Ni heterostructure

Figures 7(a) and 7(b) show the XPS spectra of the N 1s and B 1s features after CVD and after ambient exposure. Ambient exposure was accomplished by moving the sample into the chamber for ALD, isolating that chamber with the manually operated leak valves, and turning the pumps off (turbo pump and mechanical pump). This allowed the chamber to vent, filling with the ambient air from the lab, through the vent valve on the turbo pump. The sample was left in the chamber at atmospheric pressure, filled with ambient air for a minimum of 5 min before the pumps were turned back on, and the chamber was allowed to pump down to 10^{-6} Torr before being transferred back to the UHV chamber for XPS and LEED. Figure 7(a) shows a slight attenuation of N 1s intensity and the shift to lower binding energy. Both the B 1s and N 1s features exhibit shifts to lower binding energies [Figs. 7(a) and 7(b)]. Ni 2p feature [Fig. 7(c)] attenuates due to the adsorption of C and O species on the surface [Figs. 7(d) and 7(e)].

The C 1s feature [Fig. 7(d)], however, exhibits a small increase in intensity and notable broadening, as well as a diminution of the $\pi \rightarrow \pi*$ shakeup feature. There is also a substantial increase in O 1s intensity [Fig. 7(e)]. The data in Figs. 7(a)–7(c) show no evidence of direct oxidation of Ni, B, or N sites. The general shift toward lower binding energy

observed in these spectra also suggests a band bending effect induced, perhaps, by the absorption of oxygen-containing species at the graphene surface. Oxygen adsorption might lead to electron charge transfer from the substrate [graphene/h-BN/Ni(111)] resulting in the formation of an electron-depleted surface, leading to upward band bending.[53,54] Such a band bending causes binding energy shifts of both core levels and valence band toward the Fermi level (E_f). Hence, the binding energy of B 1s and N 1s shifts to lower binding energies [Figs. 7(a) and 7(b)]. Nitrogen is also an electron acceptor in BN, and therefore, the shift in the N 1s core level is higher than those observed in Ni 2p or B 1s regions.

Figure 8 shows the LEED image at 80 eV after ambient exposure and a brief (<5 min) 1000 K anneal. These data are
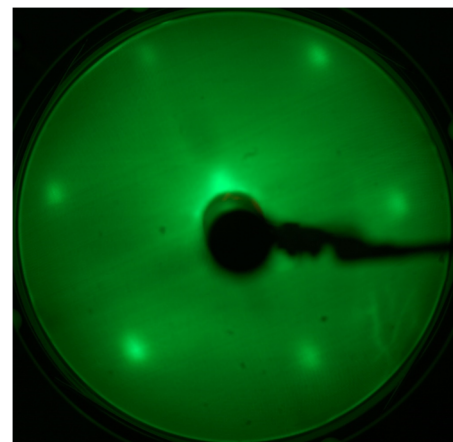

FIG. 8. LEED image, acquired at 80 eV beam energy, of graphene/h-BN/Ni heterostructure after ambient exposure and brief (<5 min) UHV anneal to 1000 K.

consistent with Fig. 6(c) demonstrating that the graphene overlayer remained intact and was ordered after a brief UHV anneal. The data in Fig. 8 also indicate that the partial oxidation observed in Fig. 7 is reversible upon annealing in UHV.

IV. SUMMARY AND CONCLUSIONS

Multilayer h-BN(0001) was grown epitaxially on Ni(111) by ALD, using sequential BCl_3/NH_3 reactions at 600 K and annealing to 1000 K in UHV. Multilayer graphene was subsequently grown on h-BN(0001) by CVD of ethylene at 1000 K. LEED shows that all three components of the graphene/BN/Ni heterostructure are in azimuthal registry. Exposure of the Ni/2 ML h-BN/3 ML graphene heterostructure to ambient resulted in some oxidation of the graphene surface, but without oxidation of Ni, B, or N sites. A brief anneal of the exposed heterostructure to 1000 K in UHV yielded the same well-defined LEED image as observed prior to exposure. The well-aligned Ni, BN, and graphene layers indicate that such heterostructures, fabricated in this manner, are suitable for various spin filters and related spintronics applications. Further, the ability to grow such heterostructures, with controlled BN and graphene thicknesses—and the resilience of these heterostructures upon exposure to ambient—indicates that devices based on these heterostructures can be produced by industrially scalable and practical methods. This provides a scalable framework for the fabrication of theoretically ideal spin filters for beyond-CMOS spintronic devices.

ACKNOWLEDGMENTS

[1]L. Ci *et al.*, Nat. Mater. **9**, 430 (2010).
[2]L. Britnell *et al.*, Nano Lett. **12**, 1707 (2012).
[3]V. M. Karpan, P. A. Khomyakov, A. A. Starikov, G. Giovannetti, M. Zwierzycki, M. Talanana, G. Brocks, J. Van Den Brink, and P. J. Kelly, Phys. Rev. B **78**, 195419 (2008).
[4]S. V. Faleev, S. S. P. Parkin, and O. N. Mryasov, Phys. Rev. B **92**, 235118 (2015).
[5]V. M. Karpan, P. A. Khomyakov, G. Giovannetti, A. A. Starikov, and P. J. Kelly, Phys. Rev. B **84**, 1 (2011).
[6]M. Morscher, M. Corso, T. Greber, and J. Osterwalder, Surf. Sci. **600**, 3280 (2006).
[7]A. Nagashima, N. Tejima, Y. Gamou, T. Kawai, and C. Oshima, Phys. Rev. Lett. **75**, 3918 (1995).
[8]C. R. Dean *et al.*, Nat. Nanotechnol. **5**, 722 (2010).
[9]G. Giovannetti, P. A. Khomyakov, G. Brocks, P. J. Kelly, and J. Van Den Brink, Phys. Rev. B Condens. Matter Mater. Phys. **76**, 073103 (2007).
[10]M. S. Driver, J. D. Beatty, O. Olanipekun, K. Reid, A. Rath, P. M. Voyles, and J. A. Kelber, Langmuir **32**, 2601 (2016).
[11]R. L. Puurunen, J. Appl. Phys. **97,** 121301 (2005).
[12]C. Bjelkevig, Z. Mi, J. Xiao, P. A. Dowben, L. Wang, W.-N. Mei, and J. A. Kelber, J. Phys. Condens. Matter **44**, 302002 (2010).
[13]D. L. Miller, M. W. Keller, J. M. Shaw, N. Chiaramonti, and R. R. Keller, J. Appl. Phys. **112**, 064317 (2012).
[14]X. Chen, B. Wu, and Y. Liu, Chem Soc. Rev. **45**, 2057 (2016).
[15]W. Gannett, W. Regan, K. Watanabe, T. Taniguchi, M. F. Crommie, and A. Zettl, Appl. Phys. Lett. **98**, 24 (2011).
[16]M. Weber, A. Julbe, A. Ayral, P. Miele, and M. Bechelany, Chem. Mater. **30**, 7368 (2018).
[17]J. A. Van Delft, D. Garcia-Alonso, and W. M. M. Kessels, Semicond. Sci. Technol. **27**, 074002 (2012).
[18]M. Weber, I. Iatsunskyi, E. Coy, P. Miele, D. Cornu, and M. Bechelany, Adv. Mater. Interfaces **5**, 1 (2018).
[19]O. Graniel, M. Weber, S. Balme, P. Miele, and M. Bechelany, Biosens. Bioelectron. **122**, 147 (2018).
[20]H. Park, T. K. Kim, S. W. Cho, H. S. Jang, S. I. Lee, and S. Y. Choi, Sci. Rep. **7**, 1 (2017).
[21]A. Pilli, J. Jones, V. Lee, N. Chugh, J. Kelber, F. Pasquale, and A. LaVoie, J. Vac. Sci. Technol. A **36**, 061503 (2018).
[22]A. Pilli, J. Jones, V. Lee, N. Chung, J. A. Kelber, F. Pasquale, and A. LaVioe, J. Vac. Sci. Technol. A **37**, 041505 (2019).
[23]M. V. Kamalakar, A. Dankert, J. Bergsten, T. Ive, and S. P. Dash, Sci. Rep. **4**, 6146 (2014).
[24]T. Yamaguchi, Y. Inoue, S. Masubuchi, S. Morikawa, M. Onuki, K. Watanabe, T. Taniguchi, R. Moriya, and T. Machida, Appl. Phys. Express **6**, 73001 (2013).
[25]M. B. Martin *et al.*, ACS Nano **8**, 7890 (2014).
[26]A. Nagashima, N. Tejima, Y. Gamou, T. Kawai, and C. Oshima, Surf. Sci. **357–358**, 307 (1996).
[27]A. B. Preobrajenski, A. S. Vinogradov, and N. Mårtensson, Phys. Rev. B **70**, 165404 (2004).
[28]A. B. Preobrajenski, A. S. Vinogradov, and N. Mårtensson, Surf. Sci. **582**, 21 (2005).
[29]A. A. Tonkikh, E. N. Voloshina, P. Werner, H. Blumtritt, B. Senkovskiy, G. Güntherodt, S. S. P. Parkin, and Y. S. Dedkov, Sci. Rep. **6**, 23547 (2016).
[30]S. Nakhaie, J. M. Wofford, T. Schumann, U. Jahn, M. Ramsteiner, M. Hanke, J. M. J. Lopes, and H. Riechert, Appl. Phys. Lett. **106**, 213108 (2015).
[31]P. Sutter, J. Lahiri, P. Zahl, B. Wang, and E. Sutter, Nano Lett. **13**, 276 (2013).
[32]N. R. Glavin, M. L. Jespersen, M. H. Check, J. Hu, A. M. Hilton, T. S. Fisher, and A. A. Voevodin, Thin Solid Films **572**, 245 (2014).
[33]M. T. Paffett, R. J. Simonson, P. Papin, and R. T. Paine, Surf. Sci. **232**, 286 (1990).
[34]A. B. Preobrajenski, M. A. Nesterov, M. L. Ng, A. S. Vinogradov, and N. Mårtensson, Chem. Phys. Lett. **446**, 119 (2007).
[35]B. Mårlid, M. Ottosson, U. Pettersson, K. Larsson, and J. O. Carlsson, Thin Solid Films **402**, 167 (2002).
[36]J. Olander, L. M. Ottosson, P. Heszler, J. O. Carlsson, and K. M. E. Larsson, Chem. Vap. Deposition **11**, 330 (2005).
[37]M. Snure, Q. Paduano, M. Hamilton, J. Shoaf, and J. Matthew Mann, Thin Solid Films **571**, 51 (2014).
[38]M. Weber, B. Koonkaew, S. Balme, I. Utke, F. Picaud, I. Iatsunskyi, E. Coy, P. Miele, and M. Bechelany, ACS Appl. Mater. Interfaces **9**, 16669 (2017).
[39]M. Weber, E. Coy, I. Iatsunskyi, L. Yate, P. Miele, and M. Bechelany, CrystEngComm **19**, 6089 (2017).
[40]J. Beatty, Y. Cao, I. Tanabe, M. S. Driver, P. A. Dowben, and J. A. Kelber, Mater. Res. Express **1**, 46410 (2014).
[41]J. Jones, B. Beauclair, O. Olanipekun, S. Lightbourne, M. Zhang, B. Pollok, A. Pilli, and J. Kelber, J. Vac. Sci. Technol. A **35**, 01B139 (2016).
[42]J. D. Ferguson, A. W. Weimer, and S. M. George, Thin Solid Films **413**, 16 (2002).
[43]M.P. Seah, in *Practical Surface Analysis*, edited by D. Briggs and M. P. Seah, 2nd ed. (Wiley, West Sussex, 1997), pp. 200–255.
[44]S. Tanuma, C. J. Powell, and D. R. Penn, Surf. Interface Anal. **35**, 268 (2003).
[45]J.A. Kelber, in *Graphene, Carbon Nanotubes, and Nanostructures Techniques and Applications*, edited by K. Morris and J. E. Iniewski (CRC, Boca Raton, FL, 2013), pp. 89–113.
[46]M. Xu, D. Fujita, J. Gao, and N. Hanagata, ACS Nano **4**, 2937 (2010).
[47]W. Hao, C. Marichy, and C. Journet, 2D Mater. **6**, 012001 (2019).
[48]J. F. Moulder, W. F. Stickle, P. E. Sobol, and K. D. Bomben, *Handbook of X-Ray Photoelectron Spectroscopy* (Perkin-Elmer Coporation, Eden Prairie, 1992).
[49]J. Park, J. C. Park, S. J. Yun, H. Kim, D. H. Luong, and S. M. Kim, ACS Nano **8**, 8520 (2014).
[50]Y. Yang, Q. Fu, M. Wei, H. Bluhm, and X. Bao, Nano Res. **8**, 227 (2014).

[51]M. Bokdam, G. Brocks, M. I. Katsnelson, and P. J. Kelly, Phys. Rev. B **90**, 085415 (2014).

[52]A. Siokou, F. Ravani, S. Karakalos, O. Frank, M. Kalbac, and C. Galiotis, Appl. Surf. Sci. **257**, 9785 (2011).

[53]Z. Zhang and J. T. Yates, Chem. Rev. **112**, 5520 (2012).

[54]Y. Y. Tay, T. T. Tan, M. H. Liang, F. Boey, and S. Li, Phys. Chem. Chem. Phys. **12**, 6008 (2010).

[55]See supplementary material at https://doi.org/10.1116/1.5120628 for detailed fitting data and additional information about process optimization.